Extremely Slow Counterion Dynamics in Xanthan Liquid Crystal through ^{23}Na and ^{14}N NMR

J. R. C. van der Maarel,*,† D. E. Woessner,‡ and M. E. Merritt‡

Leiden Institute of Chemistry, Leiden University, P.O. Box 9502, 2300 RA Leiden, The Netherlands, and Department of Radiology, Rogers Magnetic Resonance Center, The University of Texas Southwestern Medical Center at Dallas, Dallas, Texas 75235-9085

Received: November 20, 2001

To describe the structure and dynamics in a lyotropic xanthan liquid crystal, we have done ^{23}Na and ^{14}N NMR experiments. The spectra are consistent with a powder average over randomly oriented liquid-crystalline domains. From ^{14}N quadrupolar echo experiments it was concluded that the exchange among the several micron sized domains is slow with residence times in the millisecond range. Conventional spin-lock experiments (^{14}N and ^{23}Na) as well as spin-lock experiments filtered through the quadrupolar spin polarization order (^{23}Na only) revealed the existence of an extremely low frequency, submegahertz dispersion in the spectral densities pertaining to both sodium and ammonium counterions. The corresponding correlation times are on the order of tens of microseconds and agree with a structural correlation length on the order of 500 nm. The latter correlation times reflect the rearrangement of counterions among polymer segments over the same spatial extent as the polymer persistence length.

I. Introduction

NMR measurements on quadrupolar nuclei such ^{23}Na (spin $I = 3/2$) are becoming increasingly important in a wide range of applications from the investigation of soft matter such as biopolymers,[1−3] clay suspensions,[4,5] and porous materials,[6,7] through biological fluids,[8] to the diagnosis of pathology in humans via magnetic resonance imaging (MRI).[9] In the present contribution, NMR results are presented on the heterogeneous biopolymer model system of xanthan dispersed in water. Xanthan is a high molecular weight polysaccharide produced by fermentation of sugar. It is extensively used in a wide range of applications ranging from food products to secondary oil recovery. This is mostly because of its action in increasing the viscosity and control of texture and flow properties. The backbone is composed of cellulose with a trisaccharide side chain at every second residue. The side chains contain carboxyl groups that can be neutralized by sodium or ammonium. It is a rather stiff polyelectrolyte with a persistence length in the range 60−150 nm.[10,11] Furthermore, it shows a first-order phase transition to a cholesteric liquid crystal with phase boundaries between 1 and 9 wt %, depending on ionic strength.[12] In this respect, the properties of xanthan are very similar to those of DNA, because DNA also forms liquid crystals at sufficiently high packing fractions.[13,14]

The quadrupolar interaction, which is essentially a tensor property, depends on the orientation θ of the local electric field gradient in the magnetic field $\mathbf{B}_0$ of the NMR spectrometer. The instantaneous quadrupolar splitting in the spectrum is proportional to $3 \cos^2 \theta - 1$. If the motions are rapid and all θ values are equally probable, this quantity is averaged to zero so that there is no observed splitting. However, when the nucleus is in the vicinity of a macromolecule, the electric field gradient is affected through the influence of the interface of the macromolecule on its surroundings.[15] Fast local motions obviously induce high frequency fluctuations in the quadrupolar interaction. However, due to the anisotropy of the interface, these local motions do not completely average the electric field gradient to zero. The director of the residual interaction, regardless of its sources, depends on the orientation of the interface. While the nucleus is carried by diffusion to the various interfaces in solution, pertaining to either the same or different macromolecules, its residual quadrupolar interaction is undergoing changes in θ values that depend on the directors associated with these interfaces. Ions can also lose memory of the residual interaction through reorientation of the interface itself. It is clear that the latter two processes are relatively slow and characterized by rather long correlation times. If the interfaces are not randomly oriented, a nonzero value of $3 \cos^2 \theta - 1$ occurs for the nucleus in its diffusion path when averaged over a given duration. When the range of orientation order is small, the corresponding time scale over which the residual quadrupolar interaction is averaged to zero (i.e., long correlation time τ_s) is small and spectral splitting is absent. As the range of order increases, the τ_s increases; simultaneously spectral splitting becomes evident, and the spectral density of the fluctuating quadrupolar interactions at low frequency increases. Consequently, the NMR spectrum and relaxation rates of the quadrupolar probes are sensitive to the order and arrangement of macromolecules in solution through the direct effects of the macromolecule in causing nonrandom orientations of the local director.

Slow dynamics is probed by transverse relaxation or by applying a lock through an on-resonance radio frequency (rf) field. In the face of significant quadrupolar splitting, the measurement of the transverse relaxation rate becomes problematic and the spin-lock experiment is more efficient. In previous works, one of us has analyzed the relaxation of a

* Correspsonding author. Telephone: +31-715274543. Fax: +31-715274397. E-mail: j.maarel@chem.leidenuniv.nl.
† Leiden University.
‡ The University of Texas Southwestern Medical Center at Dallas.

10.1021/jp014277c CCC: $22.00
Published on Web 03/20/2002

system of spin $I = 3/2$ under (pulsed) spin locking, which allows sampling of the spectral density of the fluctuating quadrupolar interactions at a frequency on the order of the rf field strength.[16−18] This classical formalism is strictly valid, however, for nuclei in an isotropic environment, where the nuclei experience a zero average electric field gradient. More recently, we have included the static quadrupolar Hamiltonian in the calculation of the evolution of the density operator in the presence of an rf field and both static and fluctuating quadrupolar interactions.[19,20] The new formalism was subsequently used to predict the unwanted signal loss during long rf pulses in a whole-body scanner,[19] in the design of a new spin-lock method to selectively detect sodium ions in anisotropic environments,[21] and in the investigation of charged anisotropic colloids in dense Laponite suspensions.[5] For the latter system, frequency variation of the sodium spectral density in the kilohertz range was observed, from which information was derived about nematic ordering of the clay platelets.

Low frequency dispersion was also observed in the spin-lock relaxation rate of sodium in a lyotropic xanthan liquid crystal.[2] This dispersion agreed with a correlation time of 36 μs, but this information was derived with classical formalism without the inclusion of the static quadrupolar Hamiltonian.[16,18] The primary goal of the present contribution is a full analysis of the extremely slowly fluctuating electric field gradients experienced by the small counterions. This will provide an ultimate test of the spin $I = 3/2$ relaxation theory in the presence of an rf lock. We have also done ^{14}N (spin $I = 1$) quadrupolar echo experiments to estimate the residence time of ammonium ions within a domain characterized by a local director. Finally, the derived dynamic information will be interpreted in terms of structural order on the submicron distance scale, a regime that is notoriously difficult to explore with more conventional techniques such as scattering.

II. Spin 3/2 Dynamics

The formalism describing the dynamics of spin $I = 3/2$ in the presence of an rf field and both static and fluctuating quadrupolar interaction has been presented in previous work.[19,20] Two sets of coupled differential equations, of the general form $dY/dt = MY$, describe the time evolution of the density operator in the irreducible tensor operator basis. For the first set, Y is a vector of basis elements of length 8 ($Y = \{\hat{T}_{10}, \hat{T}_{11}(\mathrm{s}), \hat{T}_{21}(\mathrm{a}), \hat{T}_{22}(\mathrm{a}), \hat{T}_{30}, \hat{T}_{31}(\mathrm{s}), \hat{T}_{32}(\mathrm{s}), \hat{T}_{33}(\mathrm{s})\}$), and for the second one Y is a vector of length 7 ($Y = \{\hat{T}_{11}(\mathrm{a}), \hat{T}_{20}, \hat{T}_{21}(\mathrm{s}), \hat{T}_{22}(\mathrm{s}), \hat{T}_{31}(\mathrm{a}), \hat{T}_{32}(\mathrm{a}), \hat{T}_{33}(\mathrm{a})\}$) with $\hat{T}_{ij}(\mathrm{s})$ and $\hat{T}_{ij}(\mathrm{a})$ the symmetric and antisymmetric combinations. M is an 8×8 (7×7, respectively) matrix incorporating the effects of the static quadrupolar interaction, rf field, and relaxation. The two sets of differential equations evolve independently, but are coupled at a change of rf phase. A spin-lock field with strength B_1, and phase shifted by 90° with respect to the hard $(\pi/2)_{-y}$ preparation pulse, completely transfers the density operator in a $\hat{T}_{11}(\mathrm{a})$ state (proportional to x-magnetization). Therefore, only the second set of seven differential equations is relevant to the description of the evolution of the system under locking conditions.

Without considering relaxation, the set of seven differential equations can be diagonalized and integrated in analytical form.[19] This procedure yields three degenerate eigenvectors A_1, A_2, and A_3 with eigenvalue $\lambda_0 = 0$ and four others $A_{\pm4}$, $A_{\pm5}$ with imaginary eigenvalues $\pm i\lambda_{1,2}$, being

$$\lambda_1 = \sqrt{\omega_Q^{\,2} + 2\omega_1\omega_Q + 4\omega_1^{\,2}}$$
$$\lambda_2 = \sqrt{\omega_Q^{\,2} - 2\omega_1\omega_Q + 4\omega_1^{\,2}} \qquad (1)$$

Here, ω_Q denotes the residual quadrupolar interaction parameter measured with respect to the (local) director and ω_1 is related to the spin-lock field strength according to $\omega_1 = -\gamma B_1$. The initial single-quantum coherence, $\hat{T}_{11}(\mathrm{a})$, evolves under the spin-lock into rank-one single-quantum coherence $\hat{T}_{11}(\mathrm{a})$, quadrupolar polarization $\hat{T}_{20}$, rank-two single-quantum $\hat{T}_{21}(\mathrm{s})$ and double-quantum coherence $\hat{T}_{22}(\mathrm{s})$, rank-three single-quantum $\hat{T}_{31}(\mathrm{a})$, double-quantum $\hat{T}_{32}(\mathrm{a})$, and triple-quantum $\hat{T}_{33}(\mathrm{a})$ coherences. In particular, the spectra resulting from the Fourier transform of the transfer into the $\hat{T}_{11}(\mathrm{a})$, $\hat{T}_{20}$, $\hat{T}_{22}(\mathrm{s})$, $\hat{T}_{31}(\mathrm{a})$, and $\hat{T}_{33}(\mathrm{a})$ coherence show a prominent central resonance and two satellite pairs at frequencies λ_1 and λ_2. The satellites are liable to line-broadening effects related to rf field inhomogeneity, and accordingly, the *central* lines in the corresponding spectra are designated for relaxation studies. The line shape of the central resonance is determined by the perturbation of the null space spanned by the operators A_1, A_2, and A_3.

Including relaxation, the originally degenerate eigenvalues of the operators A_1, A_2, and A_3 cease to be degenerate and the singularity is removed (these operators are however still decoupled from $A_{\pm4}$, $A_{\pm5}$ if the line widths are much smaller than the frequencies λ_1 and λ_2). The central line is, hence, generally trimodal and consists of a narrow component related to a slowly relaxing mode and two broad components pertaining to two faster relaxing modes.[20] The rates of the fast modes are sensitive to slow molecular motion and depend on the frequencies λ_1 and λ_2 (and, hence, through eq 1 on ω_1 and ω_Q). In particular, the transfers into $\hat{T}_{20}$ and $\hat{T}_{22}(\mathrm{s})$ coherences do not exhibit a slowly relaxing mode and are bimodal. Since the evolution into $\hat{T}_{20}$ is more efficient than that into $\hat{T}_{22}(\mathrm{s})$, we will only describe theoretical results and experiments pertaining to the first one. We will also describe the conventional spin-lock experiment where the signal is detected right after the locking period without coherence transfer.

The general pulse sequence of a spin-lock experiment is thus given by

$$(\pi/2)_{\phi-90} - (\mathbf{B}_1, t_1)_\phi - (\beta)_{\phi'} - \text{detection}, t_2 \qquad (2)$$

where the final pulse is possibly included for coherence transfer. Note that the filter contains a single transfer pulse only and not the conventional pulse pair at the end of the evolution period. It is not necessary to include a mixing pulse, because the multiple-quantum coherences are already excited during the evolution under the lock. It is advisable to do two-dimensional (2D) experiments, either with or without coherence transfer. A set of spectra is obtained as a function of the spin-lock time t_1, after Fourier transformation with respect to the detection time t_2 [$F(\omega_2)$ domain]. A phase-sensitive 2D spectrum can now be obtained by taking the real part of this set and subsequent Fourier transformation with respect to the spin-lock time t_1. The signals in the $F(\omega_1)$ domain, pertaining to a certain value of ω_Q, can be selected by taking a section along $F(\omega_1)$ at the corresponding frequency in $F(\omega_2)$. As we will see below, this procedure is particularly useful in the case of an inhomogeneous distribution of the quadrupolar splitting across the sample (e.g., in the case of a powder spectrum).

In the conventional experiment, the detected signal right after the locking period includes $\hat{T}_{11}(\mathrm{a})$, $\hat{T}_{21}(\mathrm{s})$, and $\hat{T}_{31}(\mathrm{a})$ single-

TABLE 1: Relevant Amplitudes in the Relaxation Functions of the Central Resonance

	A_S	$A_{F\mp}$
$g_{11}(t)$	$\frac{1}{5}$	$\frac{1}{10}\left[\frac{{\omega_Q}^4 + 4{\omega_Q}^2{\omega_1}^2 + 64{\omega_1}^4}{{\lambda_1}^2{\lambda_2}^2} \pm \left(\frac{6{\omega_Q}^3\omega_1 q}{{\lambda_1}^2{\lambda_2}^2\sqrt{q^2+r^2}} + \frac{(\omega_Q + 4\omega_1)(\omega_Q - 4\omega_1)r}{\lambda_1\lambda_2\sqrt{q^2+r^2}}\right)\right]$
$g_{20}(t)$	0	$\frac{1}{2\sqrt{5}}\left[\frac{3\omega_Q\omega_1({\omega_Q}^2 + 4{\omega_1}^2)}{{\lambda_1}^2{\lambda_2}^2} \pm \left(\frac{({\omega_Q}^4 - 2{\omega_Q}^2{\omega_1}^2 + 16{\omega_1}^4)q}{{\lambda_1}^2{\lambda_2}^2\sqrt{q^2+r^2}} - \frac{3\omega_Q\omega_1 r}{\lambda_1\lambda_2\sqrt{q^2+r^2}}\right)\right]$
$g_{31}(t)$	$-\frac{\sqrt{3}}{5\sqrt{2}}$	$-\frac{\sqrt{3}}{10\sqrt{2}}\left[\frac{({\omega_Q}^4 - 6{\omega_Q}^2{\omega_1}^2 - 16{\omega_1}^4)}{{\lambda_1}^2{\lambda_2}^2} \pm \left(\frac{\omega_Q\omega_1({\omega_Q}^2 + 20{\omega_1}^2)q}{{\lambda_1}^2{\lambda_2}^2\sqrt{q^2+r^2}} + \frac{({\omega_Q}^2 + 4{\omega_1}^2)r}{\lambda_1\lambda_2\sqrt{q^2+r^2}}\right)\right]$

quantum coherences. After 2D Fourier transformation, the central resonance in the $F(\omega_1)$ domain contains the signal contributions originating from $\hat{T}_{11}(a)$ and $\hat{T}_{31}(a)$. The contribution related to $\hat{T}_{21}(s)$ is transformed into two satellite pairs in antiphase in $F(\omega_1)$ and does not contribute to the central resonance. Accordingly, as far as the *central* line is concerned, the locked $\hat{T}_{11}(a)$ coherence converts into

$$\hat{T}_{11}(a) \rightarrow g_{11}(t_1)\,\hat{T}_{11}(a) + g_{31}(t_1)\,\hat{T}_{31}(a) \tag{3}$$

with the real (nonoscillating) relaxation functions[20]

$$g_{ij}(t) = A_S \exp\{-R_S^{1\rho}t\} + A_{F-} \exp\{-R_{F-}^{1\rho}t\} + A_{F+} \exp\{-R_{F+}^{1\rho}t\} \tag{4}$$

and the amplitudes of interest have been set out in Table 1. The rates have the form

$$R_S^{1\rho} = J_1 + J_2$$
$$R_{F\mp}^{1\rho} = p \mp \sqrt{q^2 + r^2} \tag{5}$$

with

$$p = \frac{3{\omega_1}^2}{2}\left(\frac{J_{\lambda_2}}{{\lambda_2}^2} + \frac{J_{\lambda_1}}{{\lambda_1}^2}\right) + \frac{3}{2}J_1 + \frac{3({\omega_Q}^4 + 2{\omega_1}^2{\omega_Q}^2 + 8{\omega_1}^4)}{2{\lambda_1}^2{\lambda_2}^2}J_2$$
$$q = \frac{3{\omega_1}^2}{2}\left(\frac{J_{\lambda_2}}{{\lambda_2}^2} - \frac{J_{\lambda_1}}{{\lambda_1}^2} - \frac{4\omega_Q\omega_1}{{\lambda_1}^2{\lambda_2}^2}J_2\right)$$
$$r = \frac{(\omega_Q - 2\omega_1)(\omega_Q + 2\omega_1)}{2\lambda_1\lambda_2}(J_1 + J_2) \tag{6}$$

and are sensitive to the spectral densities at the (low) frequencies λ_1 and λ_2, and 1 and 2 times the Larmor frequency: J_{λ_1}, J_{λ_2}, J_1, and J_2, respectively. In the detection period, the single-quantum coherences evolve into (detectable) $\hat{T}_{11}(a)$ coherence according to

$$\hat{T}_{11}(a) \rightarrow \frac{1}{5}[3\cos(\omega_Q t_2)\exp(-R_s t_2) + 2\exp(-R_c t_2)]\hat{T}_{11}(a)$$
$$\hat{T}_{21}(s) \rightarrow i\sqrt{\frac{3}{5}}\sin(\omega_Q t_2)\exp(-R_s t_2)\hat{T}_{11}(a)$$
$$\hat{T}_{31}(a) \rightarrow \frac{1}{5}\sqrt{6}[\cos(\omega_Q t_2)\exp(-R_s t_2) - \exp(-R_c t_2)]\hat{T}_{11}(a) \tag{7}$$

with $R_s = J_0 + J_1 + J_2$ and $R_c = J_1 + J_2$ being the transverse relaxation rates of the satellites and the central resonance (without spin-lock field), respectively. With eq 7, the directly detected signal takes the form

$$s(t_1,t_2) = \frac{1}{5}(3g_{11}(t_1) + \sqrt{6}g_{31}(t_1))\cos(\omega_Q t_2)\exp(-R_s t_2) + (2g_{11}(t_1) - \sqrt{6}g_{31}(t_1))\exp(-R_c t_2) \tag{8}$$

The higher rank contribution g_{31} is seen to vanish if one records the (extrapolated) amplitude of the detected signal right after the spin-lock pulse ($t_2 \rightarrow 0$), or, alternatively, if one integrates the complete spectrum in the $F(\omega_2)$ domain. The $T_{1\rho}$ relaxation of the satellites and central transition in $F(\omega_2)$ is readily identified in the first and the second term on the right-hand side of eq 8, respectively. For the satellites, the amplitude of the slow mode A_S is seen to vanish in the relevant combination of the relaxation functions $3g_{11} + \sqrt{6}g_{31}$ (see Table 1). Accordingly, the $T_{1\rho}$ relaxation of the satellites is generally bimodal and is particularly sensitive to slow dynamics. The latter relaxation becomes single exponential, however, if the rf field strength far exceeds the static quadrupolar coupling $\omega_1 \gg \omega_Q$. In this limiting situation, $A_{F+} = 0$ for all coherences and the spin-lock relaxation rate of the satellites takes the simple form

$$R_{F-}^{1\rho} = \frac{3}{4}J_{\lambda_1} + J_1 + \frac{1}{4}J_2\ (\omega_1 \gg \omega_Q,\ \lambda_1 = 2\omega_1) \tag{9}$$

The spin-lock experiment can be optimized to selectively detect the quadrupolar order $\hat{T}_{20}$ by including a coherence transfer pulse and pulse-phase cycling as detailed in the Experimental Section. Including the satellites, the overall evolution of the single-quantum coherence $\hat{T}_{11}(a)$ into $\hat{T}_{20}$ during the spin-lock reads

$$\hat{T}_{11}(a) \rightarrow \left[g_{20}(t_1) - \frac{3\omega_Q\omega_1}{2\sqrt{5}}\left(\frac{\cos(\lambda_1 t_1)\exp(-R_4 t_1)}{{\lambda_1}^2} + \frac{\cos(\lambda_2 t_1)\exp(-R_5 t_1)}{{\lambda_2}^2}\right)\right]\hat{T}_{20} \tag{10}$$

with the evolution into the *central* resonance $g_{20}(t_1)$ given by eq 4. For the rates of the satellites (at frequencies λ_1 and λ_2), the reader is referred to ref 20, but they have little practical value, due to broadening effects related to rf field inhomogeneity. The evolution function g_{20} is biexponential and does not exhibit a slow mode ($A_S = 0$). The amplitudes of the fast modes are also set out in Table 1, and the rates are given by eqs 5 and 6. It can be shown that the right-hand side of eq 10 is identically zero if there is no quadrupolar coupling, as well as in the case $\omega_Q \neq 0$, but if $\omega_1 \gg \omega_Q$ or $\omega_Q \gg \omega_1$. Therefore, the rank-two zero-quantum coherence can only be created in the presence of a static quadrupolar coupling, and provided $\omega_Q \approx \omega_1$. This quadrupolar spin polarization created during the spin-lock time can be converted by a coherence transfer pulse into second-rank single quantum coherence $\hat{T}_{21}(s)$, which will evolve into detectable transverse magnetization during the detection time t_2, according to eq 7.

The present formalism has been derived for a system with uniform static quadrupolar coupling. However, as we will see below, in a xanthan liquid crystal the spectrum of sodium displays a first-order powder pattern, indicating that the coupling is intrinsically nonuniform. As for unaligned lyotropic liquid crystals,[22] we model the sample as composed of domains, each domain characterized by a local director and all of the domains having the same dynamical properties. Moreover, the exchange of ions among the domains is assumed to be slow on a time scale exceeding the inverse line widths and/or splittings, so that the observed spectrum represents a static average over all domains. Each domain is characterized by a residual quadrupolar coupling

$$\omega_Q = \bar{\omega}_Q(3\cos^2\theta - 1)/2 \tag{11}$$

where θ is the angle between the local director and the direction of the main magnetic field $\mathbf{B}_0$ and $\bar{\omega}_Q$ denotes the maximum splitting measured for $\theta = 0$. In our system all domains are randomly oriented and every value of θ is equally probable. The total NMR signal can thus be written as an integral over all orientations. In the experimental 2D spectrum, we can select, however, signals pertaining to a certain value of ω_Q by taking a slice along $F(\omega_1)$ at the corresponding frequency in $F(\omega_2)$.

In the $F(\omega_1)$ domain, the central line is composed of a sum of two Lorentzians with amplitudes and rates depending on the values of the spin-lock field strength, the static quadrupolar coupling, and the spectral densities J_{λ_1}, J_{λ_2}, J_1, and J_2. The rf power and static quadrupolar coupling can, to a very good accuracy, be obtained from the positions of the satellites. The high-frequency contributions J_1 and J_2 can be obtained from an inversion recovery experiment,[23] leaving J_{λ_1} and J_{λ_2} to be determined from a fit of the Fourier transform of g_{20} to the central line. In practice, it will be difficult to fit both spectral densities in the face of limited signal-to-noise ratio. Numerical evaluation of g_{20} shows, however, that the dependence of the line shape on J_{λ_2} is minor, but not negligible, for $\omega_Q \approx \omega_1$. For instance, in the average rate pertaining to g_{20}, which corresponds to the first cumulant, the dependence on J_{λ_2} is seen to vanish altogether for $\omega_Q = \omega_1$. Accordingly, we will carry out experiments with various spin-lock field strengths, extract spectra for which the condition $\omega_Q = \omega_1$ is satisfied, and optimize the dominant spectral density J_{λ_1} in an iterative manner as described below.

III. Experimental Section

Experiments have been performed on sodium in an aqueous solution comprising 14 wt % xanthan, 34 wt % glycerol, and 0.3 M NaCl. At 298 K, the sodium resonance shows a powder pattern with maximum static quadrupolar splitting $\bar{\omega}_Q/2\pi = 5.4$ kHz. The NMR experiments were performed with a Bruker AM-200 spectrometer equipped with a 4.7 T wide-bore superconducting magnet and a fast recovery preamplifier. A homemade probe with a solenoid coil was used. To minimize dielectric heating due to parasitic capacitance during rf irradiation, a Faraday shield (consisting of a set of parallel, isolated, wires) was mounted inside the coil and at one side connected to ground. The sample was contained in a nonspinning 10 mm outer diameter polypropylene tube. The temperature was controlled at 298 K with a fluid thermostat using Fluorinert grade FC-40 (3M Co.).

The hard ($\pi/2$) pulse duration was 9 μs, whereas the spin-lock field intensity was tuned between 0.6 and 26 kHz. The highest two spin-lock field intensities (16 and 26 kHz) were achieved with a Bruker SXP high power electron tube amplifier, whereas the lower field strength range (0.6−4.0 kHz) was covered using a BFX-5 low power transmitter. The rf carrier was adjusted exactly on resonance. Conventional spin-lock experiments were done for the two highest rf field strengths. In the case of the lower rf field strengths, the experiment was optimized to selectively detect the spin polarization quadrupolar order $\hat{T}_{20}$. For this purpose, a final coherence transfer pulse was included with optimum pulse-angle $\beta = 45°$ (see eq 2). The phase ϕ is stepped through 0°, 60°, 120°, 180°, 240°, and 300° while the receiver phase is kept at a constant value. Signal contributions originating from Zeeman order $\hat{T}_{10}$ and octopolar spin polarization $\hat{T}_{30}$ are suppressed by taking the difference of the sections along F_1 at certain positive and negative frequencies in the acquisition domain F_2 (see below). Furthermore, the cycle is supplemented with a phase alternation of the preparation pulse between +90° and −90° together with an additional 180° alternation of the receiver phase. For each experiment, 256 spectra were collected with a dwell time 10 μs and an incremental spin-lock time 25 μs. Accordingly, the sweep widths in the evolution (F_1) and detection domain (F_2) are 40 and 50 kHz, respectively. Typically, 2024 free induction decays (FIDs) per spectrum were accumulated with a repetition time of 0.2 s. A 100 Hz Lorentzian line broadening was applied prior to Fourier transformation of the FIDs.

Experiments on ^{14}N have been done in an aqueous solution comprising 17 wt % xanthan, 0.38 M NaCl, and 1.68 M NH_4Cl. The NMR experiments were performed with a Varian UNITY INOVA console equipped with an Oxford 7.05 T wide-bore superconducting magnet. A Bruker high-power broad-line probe with a solenoid coil wound on a 10 mm inner diameter Teflon form was used. The sample was contained in a 10 mm outer diameter polypropylene tube. The temperature was controlled at 298 K with an air thermostat.

The hard ($\pi/2$) pulse duration was 12.0 μs for the single-pulse, T_1, 90°−180° spin-echo, and 90°−90° solid-echo experiments; typically 512 transients were co-added. An ENI 5100L rf power amplifier was used for the conventional spin-lock experiments. The hard preparation pulse was 13.0 μs, and the rf amplitude of the spin-lock pulse was adjusted over a wide range of values. To minimize rf heating effects, only 128 co-added transients were collected at repetition times of 1 s and a maximum spin-lock time of 20 ms. A dwell time of 25 μs and a filter width of 22 kHz were employed in all experiments, and the rf carrier was adjusted exactly on resonance. The accumulated FIDs were transferred to a personal computer. The NMR signal values used in the relaxation data analysis were obtained directly from the initial values of the time domain wave forms using NUTS software.

IV. Results and Discussion

A. ^{23}Na Spin-Lock Experiments. Since for our xanthan liquid crystal the maximum static quadrupolar coupling $\bar{\omega}_Q$ = 5.4 kHz (see below), the limiting situation $\omega_1/\omega_Q \gg 1$ can only approximately be achieved for the two highest spin-lock field intensities (16 and 26 kHz). In this situation, the $T_{1\rho}$ relaxation of the satellite signals in the F_2 domain is almost monoexponential with rate eq 9. The high-frequency contributions J_1 and

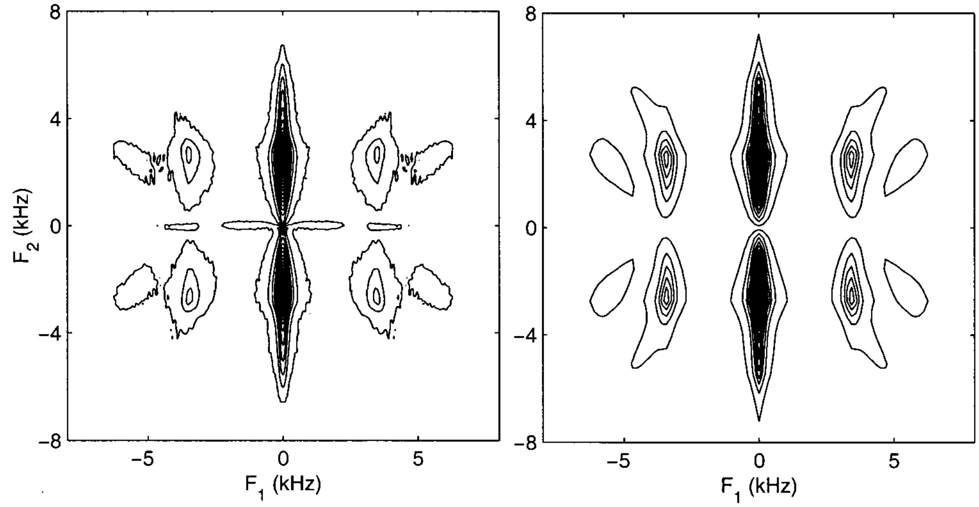

Figure 1. Left: Experimental 2D contour spectrum of the selectively detected quadrupolar order $\hat{T}_{20}$ in a xanthan solution at 298 K. The absolute value of the spectrum is displayed. Spin-lock field strength $\omega_1/2\pi = 1.95$ kHz; maximum quadrupolar splitting measured along the local director $\bar{\omega}_Q/2\pi = 5.4$ kHz. The feature along $F_2 = 0$ is due to pulse-phase imperfections. Right: The corresponding simulated spectrum.

J_2 were obtained from an inversion recovery experiment and take the values 210 and 160 s^{-1}, respectively.[23] The rates were fitted to the variation of the integrated satellite intensity as a function of the spin-lock duration, and the low-frequency spectral density can now be derived and reads $J_{2\omega_1} = 560$ and 570 s^{-1} for $\omega_1/2\pi = 16$ and 26 kHz, respectively. To check any lower frequency dispersion in the spectral density, it is desirable to extend the spin-lock experiments to lower rf field intensities.

In the moderate rf power range, the conventional $T_{1\rho}$ relaxation experiment is less eligible to extract dynamic information, because the relaxation functions become trimodal with rather complicated dependencies of the rates and amplitudes on the spin-lock field strength.[20] It is now advisable to monitor the evolution into the spin polarization quadrupolar order $\hat{T}_{20}$ (or the double quantum $\hat{T}_{22}(s)$ coherence), because it does not exhibit a slowly relaxing mode and is particularly sensitive to microsecond dynamics. We will now demonstrate the feasibility of this coherence transfer experiment and how we can extract the low-frequency spectral densities with moderate rf power for an unaligned liquid crystal displaying a first-order powder spectrum.

An experimental 2D spectrum, pertaining to the $\hat{T}_{20}$ coherence, is shown in Figure 1, together with the corresponding simulated powder pattern. The experimental spectrum was recorded with a relatively moderate rf field strength $\omega_1/2\pi = 1.95$ kHz. A typical powder average of a satellite pair in antiphase in $F(\omega_2)$ is observed (with maximum splitting $\bar{\omega}_Q = 5.4$ kHz), which is characteristic of the evolution of rank-two single-quantum coherence into observable magnetization during the detection period (see eq 7). Note that in the figure the phase information is lost, because the absolute value of the spectrum is displayed. Apart from the central resonance, the spectrum displays the two characteristic satellite pairs at frequencies $\lambda_1/2\pi$ and $\lambda_2/2\pi$ in $F(\omega_1)$. The simulated powder pattern has been calculated with the same parameters as for the experimental spectrum, including the values of the spectral densities to be determined below. In particular, the positions and shapes of the satellite signals reasonably agree with the spin-lock field strength and the powder type variation of the static quadrupolar coupling along $F(\omega_2)$.

Figure 2 displays a slice from the experimental 2D spectrum along $F(\omega_2)$ at $F_1 = 0$. The solid line represents the corresponding slice in the simulated powder pattern with optimized maximum splitting $\bar{\omega}_Q = 5.4$ kHz. Except for the intensities in the shoulder regions, the agreement is rather good, which indicates that the liquid crystal is indeed unaligned with a random orientation of the local director throughout the sample. Signals, pertaining to a certain value of the static quadrupolar interaction (e.g., originating from domains with a certain orientation), can now be selected by taking a slice from the 2D spectrum along $F(\omega_1)$ at the corresponding frequency in F_2. Some residual heterogeneity in ω_Q is unavoidable, however, due to motional line broadening effects.

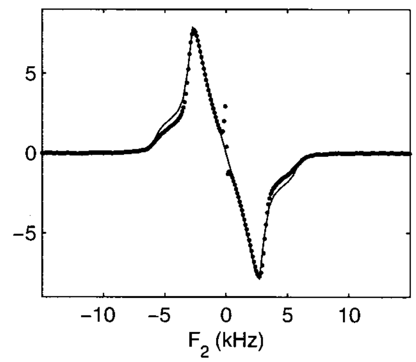

Figure 2. Experimental slice (dots) along F_2 (at $F_1 = 0$) of the selectively detected $\hat{T}_{20}$ coherence in Figure 1. The solid line represents the simulated first-order powder average of the two satellites in antiphase with maximum quadrupolar splitting $\bar{\omega}_Q/2\pi = 5.4$ kHz.

Figure 3 shows the difference of the slices along $F(\omega_1)$ at $\pm\omega_Q = \omega_1 = 1.95$ kHz in $F(\omega_2)$. In accordance with theory, the slow mode is absent in the central resonance and its shape is sensitive to the fast relaxation modes only. The spectrum is supplemented with a simplex fit of eq 10, in which the spin-lock field strengths and inhomogeneity, as well the spectral densities, are optimized. The position of the satellites is very sensitive to the spin-lock field strength. Moreover, they are particularly prone to inhomogeneous line broadening due inhomogeneity in ω_1. As a first approximation, it is assumed that the inhomogeneous broadening at the frequencies λ_i ($i = 1, 2$) is related to the $\mathbf{B}_1$ inhomogeneity $\Delta\omega_1$ according to $\Delta\omega_{\lambda_i} = |\partial\lambda_i/\partial\omega_1|\Delta\omega_1$. In the fit, the satellites were accordingly convoluted with the relevant broadening factors. Apart from the spectral densities, the spectrum was fitted with three adjustable parameters: an overall factor, a spin-lock field

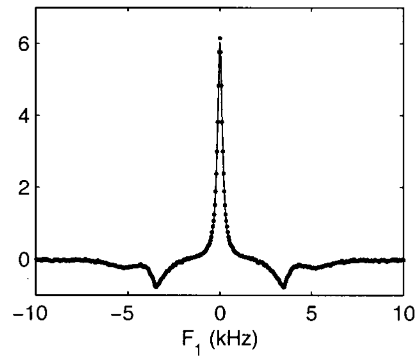

Figure 3. Experimental slice (dots) along F_1 of the selectively detected $\hat{T}_{20}$ coherence. The difference of the sections at $F_2 = \omega_1/2\pi = \pm 1.95$ kHz is displayed. Accordingly, the spectrum pertains to those domains in the powder with a splitting just matching the spin-lock field strength $\omega_Q/2\pi = \omega_1/2\pi = 1950$ Hz. The solid line represents a simplex fit.

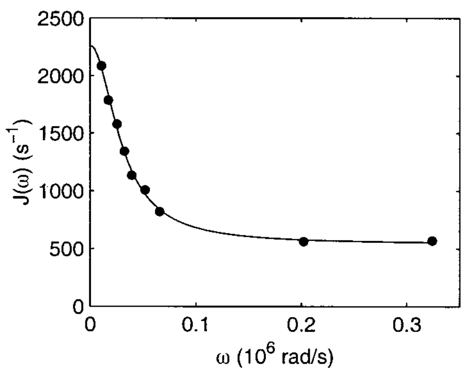

Figure 4. Spectral density (●) versus frequency. The solid line represents a fit to a sum of a Lorentzian and a constant.

strength, and a relative inhomogeneity $\Delta\omega_1/\omega_1$. Note that the spin-lock field strength and inhomogeneity, together with the static quadrupolar coupling, determine the positions and widths of the satellites. The shape of the central resonance is particularly sensitive to the values of the spectral densities in the spin-lock frequency range.

As discussed in the theoretical section, the dependence of the central line shape on J_{λ_2} is minor, but not negligible, provided $\omega_Q = \omega_1$. Accordingly, we have fitted the central line shape in an iterative manner. First, in the complete rf power range, we have analyzed the spectra neglecting the difference in spectral density at frequencies λ_1 and λ_2, i.e., we assumed $J_{\lambda_1} = J_{\lambda_2}$ ($\omega_Q = \omega_1$ was selected for each ω_1). From this series of experiments, a set of spectral densities is obtained as a function of the spin-lock field strength. In the second iteration, the assumption $J_{\lambda_1} = J_{\lambda_2}$ has been released and J_{λ_1} was optimized with interpolated values of J_{λ_2}. The interpolation was facilitated with the frequency dependence of the spectral density as given below. It was checked that after the second iteration there was no appreciable change in the fitted parameters. In this procedure, the high-frequency contributions J_1 and J_2 were fixed at their values 210 and 160 s^{-1}, respectively.

For all spin-lock field strengths, the experimental $\hat{T}_{20}$ spectra are close to the fitted curves with a single relative inhomogeneous broadening $\Delta\omega_1/\omega_1 = 0.15$. The optimized spectral densities are displayed in Figure 4, together with those obtained from the conventional spin-lock experiment at higher rf field strengths. In the low-frequency range, a systematic variation is observed, which complies with the existence of significant fluctuations on the microsecond time scale.

For a further analysis, it is necessary to introduce a specific form of the spectral density function. In biopolymer solutions there are often several independent processes at different time scales causing the loss of correlation.[2,3] Here, we will assume that there are at least three correlation times, a very short one τ_F, an intermediate one τ_M, and a longer one τ_S. The very short correlation time is related to the relatively fast dynamics of surrounding water molecules and/or other small ions, which typically occurs on a 10^{-12} s time scale. The intermediate correlation time is on the order of nanoseconds and causes dispersion in the megahertz frequency range. This correlation time is typically associated with local effects on the molecular distance scale such as diffusion of ions about polymer segments and internal polymer dynamics.[1,15] The longer correlation time on the order of microseconds is usually connected with, e.g., collective fluctuations in liquid crystals[24] or long-range diffusion of ions through a microheterogeneous polymer gel.[6] In our spin-lock frequency range, both the fast and intermediate processes are in the extreme narrowing limit, $\omega_1\tau_F \ll 1$ and $\omega_1\tau_M \ll 1$, respectively. The spectral density takes, accordingly, the form of a single Lorentzian superposed on a constant

$$J(\omega) = \frac{(2\pi)^2}{20}\left(\frac{\chi_S{}^2\tau_S}{1+\omega^2\tau_S{}^2} + \chi_M{}^2\tau_M + \chi_F{}^2\tau_F\right) = \frac{(2\pi)^2}{20}\frac{\chi_S{}^2\tau_S}{1+\omega^2\tau_S{}^2} + B \quad (12)$$

where χ_S, χ_M, and χ_F denote the root-mean-square coupling constants of the slow, intermediate, and fast processes, respectively.

From a fit of eq 12 to our data we can derive the coupling constant and correlation time of the slow process as well as the high-frequency contribution $B = \chi_M{}^2\tau_M + \chi_F{}^2\tau_F$. The solid line in Figure 4 represents a nonlinear least-squares fit with optimized parameters $\tau_S = 33 \pm 2$ μs, $\chi_S = 5.1 \pm 0.2$ kHz, and $B = 540$ s^{-1}. Excellent agreement is observed.

In the theoretical framework for analyzing these ^{23}Na experiments, it is assumed that the exchange of ions among the domains is slow on a time scale exceeding $\bar{\omega}_Q{}^{-1}$. This condition is a requirement for the observation of the resolved spectra shown in Figures 1−3.[25] Nevertheless, it is useful to obtain an estimate of this exchange rate to relate it to data from other types of physical measurements. The solid-echo rf pulse sequence refocuses the residual quadrupolar splitting, making the solid-echo amplitude especially sensitive to changes in this frequency that occur with exchange of ions among domains of different values of θ. This is like the case of attenuation of the spin-echo amplitude of a liquid molecule caused by diffusion in a magnetic field gradient. The spin-echo amplitude is much less sensitive to these changes in quadrupolar frequency because the residual quadrupolar splitting is not refocused. In the absence of this exchange, the expected decay of the solid-echo amplitude is an exponential function due to conventional transverse NMR relaxation. However, the signal after the 90°−90° solid-echo pulse sequence applied to ^{23}Na contains signal components in addition to the echo.[25] These additional components are caused by the central transition that, to first order, is unaffected by residual quadrupolar interaction and preclude the effective use of the solid-echo envelope to obtain the exchange time when a large pulse spacing is required. Fortunately, the multiple-90° rf pulse sequence with pulse spacing limited to values small compared to χ^{-1} can be used. In this way, the value 1.3 ms was obtained for τ_0, the average residence time in a given domain, from ^{23}Na NMR measurements made on a sample comprised of 20 wt % xanthan in 0.3 M NaCl.[2] For the latter

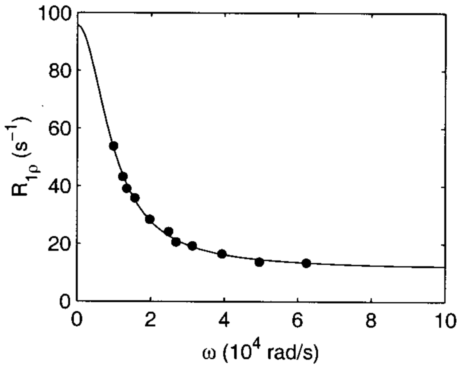

Figure 5. As in Figure 4, but for the ^{14}N spin-lock $T_{1\rho}$ relaxation rate.

sample, conventional spin-lock measurements gave $\tau_c = 36\ \mu s$; this value is very close to the one obtained in this paper from the ^{23}Na 2D spin-lock experiment (with slightly different xanthan concentration and in the presence of glycerol).

To assess the effect of exchange between domains, we have done simulations with the program ANTIOPE.[26] The parameters are set to those pertaining to the slice in Figure 3, but ANTIOPE does not include relaxation effects. Nevertheless, it was found that exchange with an average domain residence time of 1.3 ms broadens the peak by only around 100 Hz, indicating that the assumption of no exchange in the formalism applies well to these ^{23}Na spin-lock NMR experiments.

The above delineated limitations to the use of the solid-echo do not apply to spin $I = 1$ nuclei, such as ^{14}N and ^{2}H, because integer-spin nuclei do not have a central transition. Accordingly, we have done supplementary ^{14}N NMR experiments to obtain a better estimate of the domain residence time of NH_4^+ ions in an otherwise similar lyotropic xanthan liquid crystal.

B. Results from 1D Experiments on ^{14}N. The single-pulse FID and the spin-echo envelope for ^{14}N in the 17 wt % xanthan sample appear identical, indicating that $\mathbf{B}_0$ inhomogeneity is unimportant in these measurements. The initial portions of these curves indicate a powder pattern with an effective residual quadrupolar coupling constant ($\chi = e^2qQ/h$) of approximately 784 Hz. For comparison, the ^{23}Na signal from this sample has $\chi = 4.0$ kHz. Interestingly, these values are comparable to the ^{14}N and ^{23}Na quadrupolar splittings of 910 Hz and 4.0 kHz, respectively, observed in the NMR spectra of a lamellar lyotropic system containing ammonium and sodium ions (33.8 wt % ammonium decyl sulfate, 5.4% decanol, 1.8% methanol, 5.4% Na_2SO_4, and 53.6% D_2O).[27]

The T_1 value obtained from the inversion recovery experiment is 121 ms. This relatively large value ensures that the high-frequency contributions J_1 and J_2 do not strongly affect the behavior of the transverse magnetization.

Conventional spin-lock $T_{1\rho}$ experiments with rf field strengths $\omega_1/2\pi$ ranging from 1.57 to 9.93 kHz were done. The relaxation curves appear monoexponential. The relaxation rates were analyzed with the relationship that is similar to eq 12 (but pertaining to spin $I = 1$)[28]

$$R_{1\rho}(\omega_1) = \frac{9\pi^2}{20}\frac{\chi^2\tau_c}{1 + 4{\omega_1}^2{\tau_c}^2} + B \qquad (13)$$

where χ is the quadrupolar coupling constant of the relaxation interaction and B is a constant. A fit of this equation to the data yields $\tau_c = 51 \pm 4\ \mu s$, $\chi = 610 \pm 7$ Hz, and $B = 11.4 \pm 0.7\ s^{-1}$. A plot of the data and the fitted curve is displayed in Figure 5. The value of the correlation time pertaining to the ammonium ion is close to the one for the sodium low-frequency dispersion ($\tau_S = 33 \pm 2\ \mu s$). This shows that the ammonia and sodium ions are involved in similar dynamical processes.

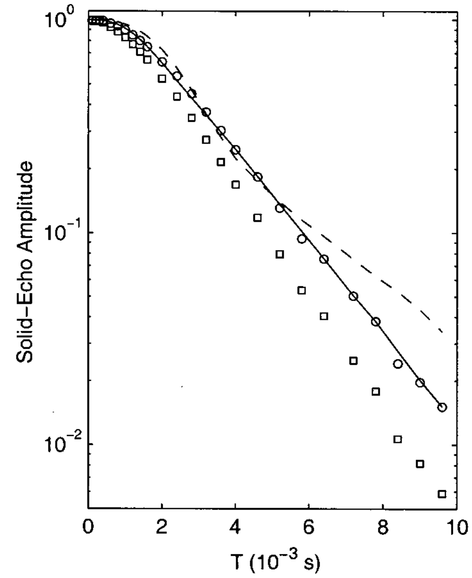

Figure 6. Solid-echo envelopes for ^{14}N NMR experiments. The experimental (□) and relaxation-adjusted (○) amplitudes at $T = 2\tau$ are displayed. The solid line is the simulated random-jump envelope calculated with $\chi = 784$ Hz and $\tau_0 = 1.8$ ms. The dashed line is the simulated rotational diffusion envelope calculated with $\chi = 745$ Hz and $\tau_0 = 4.03$ ms. Note that the simulated curves and the experimental relaxation-adjusted curve coincide at $T = 3.2$ ms, the time at which the normalized amplitude of the relaxation-corrected curve is equal to e^{-1}.

Both the 90°−180° spin-echo and the 90°−90° solid-echo envelopes are affected by the residual χ and the residence time τ_0 that describes the changes in the quadrupolar frequency that occur while the nucleus migrates to different domains. The resulting signals are, however, different, because the solid-echo sequence refocuses the residual quadrupolar splitting whereas the spin-echo sequence does not. Consequently, the use of both echo envelopes pertaining to spin $I = 1$ nuclei enables us to determine the residual χ and τ_0.[29−31] To do this, it is necessary to use measured envelopes that are corrected for transverse relaxation. The latter correction is facilitated by the spin-lock experiment: from eq 13 and the fitted parameters the rate of transverse relaxation in the absence of a spin-lock field can be calculated and reads $R_{1\rho}(\omega_1{=}0) = R_2 = 95.5\ s^{-1}$.

The experimental solid-echo amplitudes of ^{14}N are shown in Figure 6. The solid-echo envelope is a relatively long monotonic decay, because the quadrupolar splitting is refocused at the time of the echo peak.[31,32] The corrected experimental solid-echo amplitudes of ^{14}N are shown in Figure 6. Clearly, the initial points do not follow an exponential decay, indicating significant echo amplitude attenuation from exchange among different domains. As shown in Figure 6, the corrected solid-echo amplitudes are in excellent agreement with a strong-collision model in which the successive domains encountered by an ammonium ion have a random orientation compared to that of the domain exited (random jump model).[25,30,31] This fit of the model to the data is obtained with $\tau_0 = 1.8$ ms and $\chi = 784$ Hz. Fitting these amplitudes to a weak-collision model in which the successive domains differ little in orientation (rotational diffusion model) provides an inferior fit to the data.[32] These two models predict a different time dependence of the solid-echo amplitude that is readily apparent at times less than the time required for the curve to decay to e^{-1} of the initial amplitude at time $t = 0$.[33]

Since this value of τ_0 is on the same order of magnitude as the spin-lock times, the possibility that exchange causes an increase in the $R_{1\rho}(\omega_1)$ values was checked by use of ANTIOPE.[26] For the values of ω_1 employed in these conventional spin-lock experiments, any affects of exchange were found to be very small.

Residence times in the millisecond range also occur in the ^{2}H (spin $I = 1$) solid-echo curves of xanthan samples prepared with deuterium oxide and exhibit residual quadrupolar splitting in the ^{2}H resonance.[30] The deuterium experiments also agree with the random jump model much better than with the rotational diffusion model.[25,31,32] The τ_0 value in a sample comprised of 20 wt % xanthan in D_2O was found to be 5.5 ms.[30] However, these spin-echo and solid-echo data were not corrected for transverse relaxation by use of spin-lock measurements, resulting in an uncertainty in the τ_0 value obtained from them.

V. Conclusion

With a view to characterize the dynamics of small ions in a xanthan lyotropic liquid crystal, we have done ^{23}Na and ^{14}N spin-lock NMR experiments. The observation of the resolved spectra shown in Figures 1−3 indicates that the exchange of sodium ions among domains with a different orientation of the local director is slow on a time scale exceeding $\bar{\omega}_Q^{-1}$. ^{14}N solid (quadrupolar) echo experiments on the ammonium (NH_4^+) ion give a domain residence time of 1.8 ms, which is indeed an order of magnitude longer than the inverse sodium quadrupolar splitting. Residence times in the millisecond range are consistent with a diffusing water molecule or a hydrated ion remaining in a micron-sized domain before it enters a different domain. With a typical diffusion coefficient of 10^{-9} m^2/s, one derives a typical domain correlation length on the order of 3 μm. This size is also consistent with micron-size birefringence domains observed in polarized light microscopy textures.

The spin-lock experiments reveal extremely low frequency, submegahertz, dispersion in the spectral density pertaining to both Na^+ and NH_4^+ counterions. As far as we are aware, the present experiments give exclusive evidence of the existence of such slow fluctuations experienced by small ions in biopolymer solutions. The derived correlation times for both ions are similar and are on the order of tens of microseconds. Since the electric field gradient experienced by ^{14}N is almost completely of intramolecular origin, this similarity in correlation times strongly suggests that the dominant fluctuating electric field gradients driving Na^+ relaxation originate from temporal distortions of the ion hydration complex. In our lyotropic liquid crystal, the origin of these temporal distortions lies presumably in, e.g., rearrangements of relatively large polymer segments and/or diffusion along the polymer contour over distances on the order of the persistence length. In this context, it is of interest to calculate the mean-square displacement during a time lapse of a single correlation time. With a typical diffusion coefficient of 10^{-9} m^2/s, one derives a correlation length on the order of 500 nm. The latter value compares favorably to reported values for the persistence length in the range 60−150 nm.[10,11] It is clear that the submegahertz frequency dispersion is related to structural order on the submicron distance scale.

The relatively small value of the mean square coupling constant of the slowly fluctuating electric field gradients results in moderate relaxation rates despite the relatively long correlation times. Changes in the density operator are accordingly still small on the time scale of the lattice motions, which is a necessary condition for the applicability of Redfield perturbation theory. Compared to conventional spin-lock $T_{1\rho}$ experiments, the present method allows the use of significantly smaller ω_1 values to obtain correct values of even longer correlation times. Also, it more readily enables one to check whether there is a dependence of spectral density on domain orientation. However, there may be an upper limit to the correlation time that can be obtained by use of either method.

Acknowledgment. We thank Drs. A. Delville and I. Hancu for stimulating discussions. Part of this work was supported by NIH-RR-02584.

References and Notes

(1) Groot, L. C. A.; van der Maarel, J. R. C.; Leyte, J. C. *J. Phys. Chem.* **1994**, *98*, 2699.

(2) Woessner, D. E. *Concepts Magn. Reson.* **2001**, *13*, 294.

(3) Stein, V. M.; Bond, J. P.; Capp, M. W.; Anderson, C. F.; Record, M. T. *Biophys. J.* **1995**, *68*, 1063.

(4) Delville, A.; Porion, P.; Faugère, A. M. *J. Phys. Chem. B* **2000**, *104*, 1546.

(5) Porion, P.; Al Muhktar, M.; Meyer, S.; Faugère, A. M.; van der Maarel, J. R. C.; Delville, A. *J. Phys. Chem. B* **2001**, *105*, 10505.

(6) Tromp, R. H.; van der Maarel, J. R. C.; de Bleijser, J.; Leyte, J. C. *Biophys. Chem.* **1991**, *41*, 81.

(7) Meersmann, T.; Smith, S. A.; Bodenhausen, G. *Phys. Rev. Lett.* **1998**, *80*, 1398.

(8) Eliav, U.; Navon, G. *J. Magn. Reson. B* **1994**, *103*, 19.

(9) Hilal, S.; Oh, C.; Mun, I.; Silver, A. In *Magnetic Resonance Imaging*; Stark, D., Bradley, W., Eds.; Mosby: St. Louis, 1992.

(10) Gamini, A.; Mandel, M. *Biopolymers* **1994**, *34*, 783.

(11) Berth, G.; Dautzenberg, H.; Christensen, B. E.; Harding, S. E.; Rother, G.; Smidsrod, O. *Macromolecules* **1996**, *29*, 3491.

(12) Sato, T.; Kakihara, T.; Teramoto, A. *Polymer* **1990**, *31*, 824.

(13) Kassapidou, K.; Jesse, W.; van Dijk, J. A. P. P.; van der Maarel, J. R. C. *Biopolymers* **1998**, *46*, 31.

(14) Kassapidou K.; van der Maarel, J. R. C. *Eur. Phys. J. B* **1998**, *3*, 471.

(15) Chen, S. W. W.; Rossky, P. J. *J. Phys. Chem.* **1993**, *97*, 10803.

(16) van der Maarel, J. R. C. *J. Chem. Phys.* **1989**, *91*, 1446.

(17) van der Maarel, J. R. C.; Tromp, R. H.; Leyte, J. C.; Hollander, J. H.; Erkelens, C. E. *Chem. Phys. Lett.* **1990**, *169*, 585.

(18) van der Maarel, J. R. C. *J. Chem. Phys.* **1991**, *94*, 4765.

(19) Hancu, I.; van der Maarel, J. R. C.; Boada, F. E. *J. Magn. Reson.* **2000**, *147*, 179.

(20) van der Maarel, J. R. C.; Jesse, W.; Hancu, I.; Woessner, D. E. *J. Magn. Reson.* **2001**, *151*, 298.

(21) Hancu, I.; van der Maarel, J. R. C.; Boada, F. E. *Magn. Reson. Med.* **2002**, *47*, 68.

(22) Boden N.; Jones, S. A. In *Nuclear Magnetic Resonance of Liquid Crystals*; Emsley, J. W., Ed.; Reidel: Dordrecht, 1985.

(23) van der Maarel, J. R. C. *Chem. Phys. Lett.* **1989**, *155*, 288. The longitudinal relaxation rate of the satellites is monoexponential with rate $R_{1,s} = 2J_2$. The longitudinal rate of the central resonance is biexponential with equal fractions and rates $R_{1,c1} = J_1$ and $R_{1,c2} = J_2$. For a small difference in J_1 and J_2, the central line can be fitted to a single exponential with an average rate $R_{1,c} = J_1 + J_2$.

(24) Heaton, N.; Reimer, D.; Kothe, G. *Chem. Phys. Lett.* **1992**, *195*, 448.

(25) Woessner, D. E.; Bansal, N. *J. Magn. Reson.* **1998**, *133*, 21.

(26) Stickney de Bouregas, F.; Waugh, J. S. *J. Magn. Reson.* **1992**, *96*, 280.

(27) Charvolin, J.; Loewenstein, A.; Virlet, J. *J. Magn. Reson.* **1977**, *26*, 529.

(28) van der Maarel, J. R. C. *J. Chem. Phys.* **1993**, *99*, 5646.

(29) Woessner, D. E.; Snowden, B. S., Jr. *J. Chem. Phys.* **1969**, *50*, 1516.

(30) Woessner, D. E.; Snowden, B. S., Jr. *Ann. N. Y. Acad. Sci.* **1973**, *204*, 113.

(31) Woessner, D. E. *Mol. Phys.* **1977**, *34*, 899.

(32) Woessner, D. E.; Snowden, B. S., Jr.; Meyer, G. H. *J. Chem. Phys.* **1969**, *51*, 2968.

(33) Pfitsch, D. W.; McDowell, A. F.; Conradi, M. S. *J. Magn. Reson.* **1999**, *139*, 364.